Journal of Power Sources 274 (2015) 15–21

Contents lists available at ScienceDirect

Journal of Power Sources

journal homepage: www.elsevier.com/locate/jpowsour

The lithium ion capacitor with a negative electrode of lithium titanium zirconium phosphate

Chien-Ju Peng, Dah-Shyang Tsai*, Chuan-hua Chang, Hao-Yu Wei

Department of Chemical Engineering, National Taiwan University of Science and Technology, 43, Keelung Road, Section 4, Taipei 10607, Taiwan

HIGHLIGHTS

- A hybrid capacitor made of $LiTi_{1.5}Zr_{0.5}(PO_4)_3$ negative and AC positive electrodes.
- The crystallite size of LTZP with a nasicon structure is 36 nm.
- OCP at 0% SOC is critical for charge/discharge performance of the capacitor.
- At low currents the capacitor behavior is dominated by its negative electrode.

ARTICLE INFO

Article history:
Received 18 April 2014
Received in revised form
6 October 2014
Accepted 6 October 2014
Available online 16 October 2014

Keywords:
Lithium ion capacitor
Lithium titanium zirconium phosphate
Nanoparticles
Activated carbon
Hybrid capacitor

ABSTRACT

Nanoparticles of $LiTi_{1.5}Zr_{0.5}(PO_4)_3$ ($LT_{1.5}Z_{0.5}P$) with a nasicon-type structure have been prepared through a sol–gel modified pechini method, which allows a low synthesis temperature and yields a small crystallite size of 36 nm. When implemented as the negative electrode in a hybrid capacitor, $LT_{1.5}Z_{0.5}P$ exhibits a sizable lithium capacity of 6–4 mol below 2.0 V *vs.* Li/Li^+. But the actual capacity being exploited depends on the position of open circuit potential (OCP) at 0% state of charge (SOC). For the capacitor with a 1:1 mass ratio of $LT_{1.5}Z_{0.5}P$ over activated carbon (AC), OCP at 0% SOC generally decreases with increasing mass-specific current and voltage window size, varying between 2.0 and 1.5 V *vs.* Li/Li^+. Hence the $LT_{1.5}Z_{0.5}P$ electrode surpasses the AC electrode in capacitance at high currents, leading to the $LT_{1.5}Z_{0.5}P$/AC capacitor behaves similar to a double layer capacitor. Conversely, the $LT_{1.5}Z_{0.5}P$/AC capacitor exhibits more battery-like traits at low specific currents. The maximum energy density of this hybrid cell measures 46.7 Wh kg^{-1} at voltage window 3.4 V and specific current 70 mA g^{-1}.

1. Introduction

The lithium ion capacitor is a hybrid capacitor that implements the battery electrode, mostly relying on intercalation or insertion chemistry of lithium ions, in one of the two electrodes to augment the cell energy density. The other electrode depends on the double-layer capacitance of high-surface-area carbons for rapid energy cycling [1–3]. Given the energetic but sluggish characters of battery kinetics, the quality of high power performance is traded for energy capacity, resulting in a relatively new member in the capacitor family based on electrochemistry. Therefore it is essential to understand the capacitor features of charge/discharge capacity and cycle stability through examining the test cell performance.

The concept of hybrid capacitor has been applied to many cells including both organic and water-based electrolytes. Organic electrolytes provide a wider working potential window, while aqueous electrolytes are safer and more eco-friendly. Several cathode compositions have been investigated as the positive electrode for capacitor, including $LiMn_2O_4$ or $LiNi_xMn_{2-x}O_4$ [4–7], $LiFePO_4$ [8,9], $LiCoO_2$ [10,11], Li_2MnSiO_4 [12], $LiVPO_4F$ [13], $Li_3V_2(PO_4)_3$ [14], V_2O_5 and VO_2 [15]. These electrodes of high potential plateau promote the storage capacity rating. Yet it is the performance of non-aqueous cells with a negative lithium storage electrode sets the hybrid capacitor apart from conventional supercapacitors. The two leading negative electrodes are $Li_4Ti_5O_{12}$ and lithiated graphite [2]. $Li_4Ti_5O_{12}$ is a renowned anode composition for lithium ion battery. It superior properties include a sizeable capacity 175 mAh g^{-1} (theoretical value), a high coulombic efficiency, little volume change involved in ion insertion, and a flat discharge profile at 1.55 V *vs.* Li/Li^+. Its shortcomings are low ion conductivity and poor electronic conductivity, also a relatively narrow potential window (generally <3.2 V), confined by its well-defined ion insertion potential [3,16–20]. On the other hand, the

* Corresponding author. Tel.: +886 2 27376618; fax: +886 2 27376644.
E-mail address: dstsai@mail.ntust.edu.tw (D.-S. Tsai).

http://dx.doi.org/10.1016/j.jpowsour.2014.10.047
0378-7753/

pre-lithiated graphite effects a wider working potential window, >4.0 V, when it is paired with a positive electrode of double-layer capacitance. During the capacitor operation, the potential of graphite electrode remains flat around 0.1 V (*vs.* Li/Li^+), and the capacitor charges and discharges at relatively high levels of SOC (state of charge) to maintain the high power attributes [21–23].

$LiTi_{2-x}Zr_x(PO_4)_3$ (LTZP) may be viewed as a variant of $LiTi_2(PO_4)_3$ (LTP). Both belong to the nasicon family that crystallizes in rhombohedral structure with $R\bar{3}\ c$ space group. Considerable research efforts have been devoted to LTP and its associated solid solutions to exploit its potential as negative electrode [24–28]. LTP is known to allow insertion of 2 mol lithium at 2.5 V *vs.* Li/Li^+. Unfortunately, the 2.5 V plateau is awkward to implement since this plateau potential is too high for the negative electrode and too low for the positive electrode in a capacitor. In this work, we study the lithium ion insertion of LTZP underneath this potential plateau, and construct a hybrid capacitor with an LTZP negative electrode and a positive activated carbon (AC) electrode. Our collected charge/discharge data shows that the quality of performance is respectable when this battery-like electrode is operated below its potential plateau in the full cell configuration.

2. Experimental

Compounds of general formula $LiTi_{2-x}Zr_x(PO_4)_3$, with $x = 0.2$, 0.5, and 0.8, were synthesized through the sol–gel modified Pechini method. They were abbreviated as $LT_{1.8}Z_{0.2}P$, $LT_{1.5}Z_{0.5}P$, and $LT_{1.2}Z_{0.8}P$. The preparation procedure began with dissolution of 4.69 g titanium isopropoxide in 120 ml solution of 30% hydrogen peroxide, followed by mixing with another 60 ml solution of 35% ammonia water. The mixing persisted until the solution looked transparent, then 3.81 g citrate acid was added in. The solution so obtained was mixed with another solution containing 200 ml water, 0.53 g lithium carbonate (Li_2CO_3, 30% excess), 0.98 g zirconium oxychloride ($ZrOCl_2$), and 3.80 g monoammonium phosphate ($NH_4H_2PO_4$). All reagent-grade chemicals were purchased from Aldrich. The resulting mixture was slowly heated up to 80 °C, meanwhile, 1.02 g ethylene glycol was added with continuous stirring. After the solution had thickened and gelled, its temperature was further raised to 240 °C, and the gel decomposed into black powder. The black powder was finally calcined at 800 °C in air for 12 h to obtain a white powder of LTZP, which had a stoichiometric ratio of Li:Ti:Zr:P = 1:1.5:0.5:3, $LT_{1.5}Z_{0.5}P$. We deliberately kept the synthesis temperature low to prevent crystallite growth and minimize lithium evaporation. To make LTZP conductive, 5 wt% of Super P carbon black (TIMCAL) and 95 wt% $LT_{1.5}Z_{0.5}P$ were blended in, then ball-milled in a plastic jar with zirconia balls for 12 h. The resulting powder mixture was denoted as c-$LT_{1.5}Z_{0.5}P$, which was the major ingredient of negative electrode.

Electrochemical measurements were performed using two MikroMasch electrochemical test cells (SC-Basic, MikroMasch). Each cell had a spring, exerting a 20-N compressive force on the electrodes. The cell is reusable. Its assembly and measurements were carried out in an argon-filled glove box (GB-100, SunRay Science). The glove box was equipped with a load lock vacuum chamber and a gas circulating/purifying system to keep oxygen and water impurity <1 ppm. The LTZP electrode was prepared with 80 wt% of c-LTZP (containing 95 wt% LTZP), 10 wt% of Vulcan carbon (Cabot), and 10 wt% of PVdF binder (Aldrich). These ingredients were homogenized with a suitable amount of 1-methyl-2-pyrrolidinone (NMP) solvent to form a paste, which was dispersed on a pre-weighed copper disk of 20 mm in diameter, and dried at 80 °C in a vacuum oven to remove the solvent. The dried LTZP electrode was cold pressed under 1.5 ton force, and weighed again to calculate the active materials mass. The AC electrode was prepared in the same manner, except that the AC paste was applied onto an aluminum disk of 20 mm in diameter. The dried AC electrode contained 80 wt% of activated carbon (grade 4/70, 3J&J Pharma Pte Ltd), 10 wt% of Vulcan carbon, and 10 wt% of PVdF binder.

The LTZP/AC hybrid capacitor was assembled with a negative LTZP electrode and a positive AC electrode, separated by a 25 μm thick microporous membrane (Celgard 2500) and 1.0 M electrolyte of $LiPF_6$ in ethylene carbonate (EC) and dimethyl carbonate (DMC) solution (50:50 by volume, LB-301 Zhangjiangang Guotai-Huarong New Chemical Materials). Electrochemical measurements were conducted after electrolyte completely wetted the two electrodes. The wetting was ensured approximately 12 h after the cell was assembled. A number of capacitors were fabricated with three $LT_{1.5}Z_{0.5}P$:AC mass ratios, including 1:0.5, 1:1, and 1:2. Our study was centered on the 1:1 mass ratio, denoted as $LT_{1.5}Z_{0.5}P$/AC (1:1) cell. Before recording the galvanostatic charge/discharge data, we measured the electrode potential variations under various conditions, using a three-electrode setup. In the three-electrode setup, a small piece of lithium metal was placed as reference electrode on the same side of the positive electrode, without touching the positive. Both the cell voltage and the negative potential were recorded simultaneously after the cell run steadily in ~10 cycles. The positive potential was calculated as the sum of cell voltage and negative potential. Then, we measured the capacity and cycle stability data with the two-electrode setup. In the capacity study, we chose the cell that operated steadily, measured and reported the third-cycle performance of a given voltage window with various specific currents. In the cycle stability measurement, we monitored the $LT_{1.5}Z_{0.5}P$/AC (1:1) cell performance in 100 cycles at low specific currents. One measurement lasted for 6 or 7 days.

Two half cells, $Li/LT_{1.5}Z_{0.5}P$ and Li/AC, were also assembled in the same manner with a lithium metal foil (99.9% purity, Alfa Aesar) of 20 mm in diameter. Cyclic voltammetric (CV) studies of AC electrode capacity were performed with the Li/AC cell, and data were collected using a potentiostat (5000 Workstation, Jiehan). Other data of galvanostatic charge/discharge experiments and cycle stability were recorded with a multichannel potentiostat (1470E, Solartron).

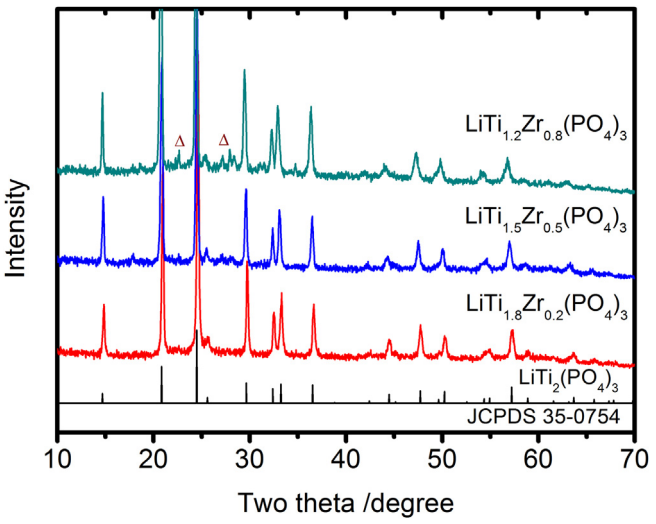

Fig. 1. X-ray diffraction patterns of $LT_{1.8}Z_{0.2}P$, $LT_{1.5}Z_{0.5}P$, $LT_{1.2}Z_{0.8}P$. Powders of the LTZP compositions have been calcined at 800 °C for 12 h. The diffraction peaks exclusively belong to the nasicon crystal, except those minor ones marked with the upright triangles.

Nitrogen adsorption–desorption isotherms of AC were measured using a surface area and pore size analyzer (AUTOSORB-1, Quantachrome). The Brunauer-Emmett-Teller (BET) surface area along with Barrett-Joyner-Halenda (BJH) pore size and volume were calculated with the software AS1Win version 2.01. The crystal structure of LTZP nanoparticles was analyzed using an X-ray diffractometer (D2 Phaser, Bruker) which was equipped with a copper Kα radiation source (wavelength 0.15406 nm) and nickel filter. Fitting of lattice parameters was performed with the free software UnitCellWin, written by Holland and Redfern. Particle morphology was examined using a scanning electron microscope (SEM, JSM-6500F, JEOL).

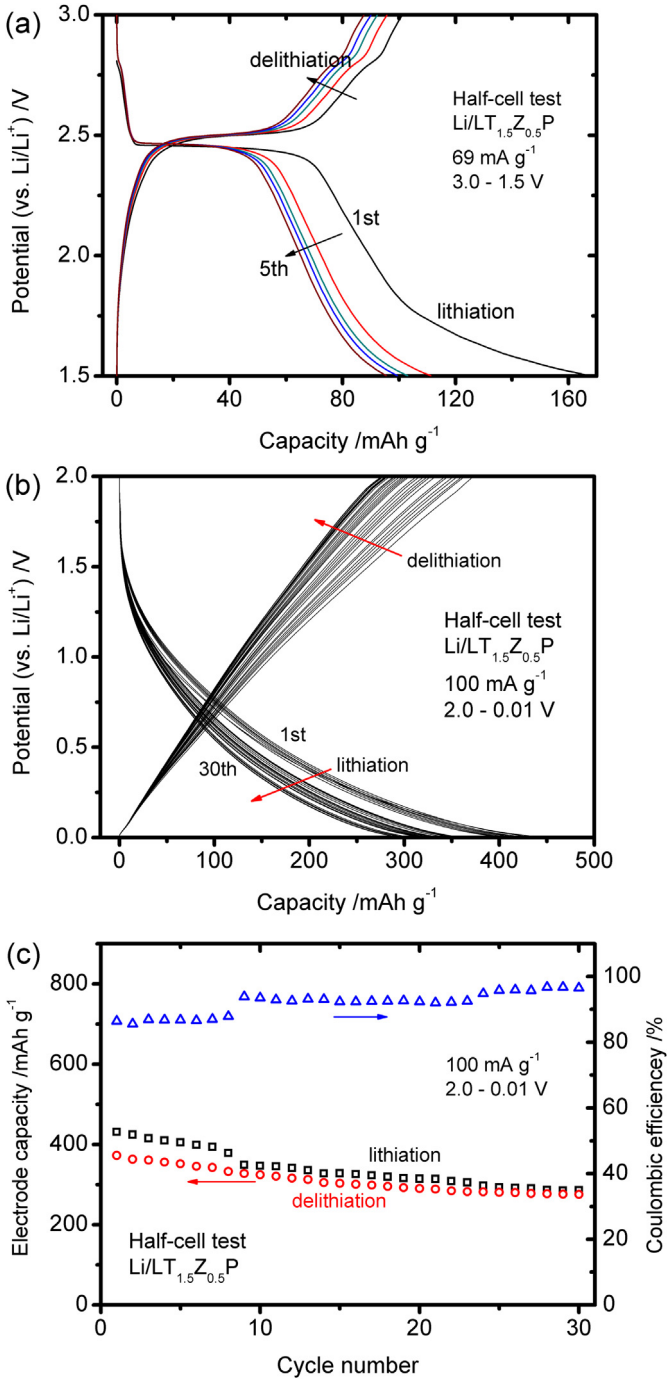

Fig. 2. Lithiation/delithiation of $LT_{1.5}Z_{0.5}P$ in the Li/$LT_{1.5}Z_{0.5}P$ half cell. (a) Five cycles of lithiation/delithiation are plotted with respect to $LT_{1.5}Z_{0.5}P$ capacity between 3.0 and 1.5 V (*vs.* Li/Li^+) at 69 mA g^{-1} (1.05 C). (b) Thirty cycles of lithiation/delithiation are plotted with respect to $LT_{1.5}Z_{0.5}P$ capacity between 2.0 and 0.01 V (*vs.* Li/Li^+) at 100 mA g^{-1} (1.53 C). (c) A plot summarizes the capacity fading and the coulombic efficiency variation in (b).

3. Results and discussion

3.1. Properties of active materials and electrodes

Using the sol–gel modified Pechini method, we manage to synthesize LTZP powders at 800 °C, which is ~200 °C less than the conventional preparation temperature of LTP powder. Fig. 1 presents the distinct diffraction lines of nasicon crystal for three compositions, which contain 10, 25, 40 mol% of zirconium. The three diffraction patterns of LTZP solid solutions show a consistent shifting in peak position toward lower angles with increasing zirconium content. The low-angle shifting signifies an expansion in the unit cell dimensions, because the Zr^{4+} ion of larger size substitutes for the Ti^{4+} ion. Fitting the peak positions to a hexagonal structure verifies the above conjecture. The fitted lattice parameters are, $a = 0.8491$ nm, $c = 2.0889$ nm for $LT_{1.8}Z_{0.2}P$; $a = 0.8496$ nm, $c = 2.1048$ nm for $LT_{1.5}Z_{0.5}P$; $a = 0.8572$ nm, $c = 2.1128$ nm for $LT_{1.2}Z_{0.8}P$. Lattice expansion through zirconium substitution has been reported to enhance the lithium mobility during ion insertion [29], which ought to benefit power performance of the hybrid capacitor. Among the three LTZP compositions, we focus attention on the composition of $LT_{1.5}Z_{0.5}P$ and study its feasibility as the negative electrode for hybrid capacitor. Selection of $LT_{1.5}Z_{0.5}P$ is based on the following considerations. When the zirconium content is low, 10 mol%, the composition comes close to $LiTi_2(PO_4)_3$ that has been extensively studied in literature [26–28]. When the zirconium content is high, 40 mol%, three diffraction lines of an impurity phase emerge at $2\theta = 22.7°$, 27.2°, 28.0°. The impurity phase is difficult to eliminate, because high zirconium content increases the compound refractoriness and lithium tends to evaporate at high temperatures. On the other hand, the chosen $LT_{1.5}Z_{0.5}P$ has sufficient zirconium and relatively easy in synthesis. The crystallite size of as-prepared $LT_{1.5}Z_{0.5}P$ is 36 nm, estimated with the strongest diffraction line at $2\theta = 24.5°$ and the Scherrer formula $0.9\lambda/\beta\cos\theta$, in which λ is the wavelength, β is the full width at half maximum of the Bragg angle θ.

The lithium capacity of $LT_{1.5}Z_{0.5}P$ is measured using a Li/$LT_{1.5}Z_{0.5}P$ half cell. Fig. 2(a) shows the lithiation/delithiation curves of $LT_{1.5}Z_{0.5}P$ at 69 mA g^{-1} between 3.0 and 1.5 V (*vs.* Li/Li^+). The lithiation curve displays a distinct plateau at 2.45 V, while the delithiation curve shows a plateau at 2.50 V (*vs.* Li/Li^+). The plateau capacity of the first delithiation cycle is estimated ~59 mAh g^{-1}, equivalent to 0.90 mol of lithium, since the insertion of 1 mol of lithium corresponds to 65.5 mAh g^{-1} for $LT_{1.5}Z_{0.5}P$. The plateau capacity drops to 51 mAh g^{-1} (0.78 mol Li) in the second delithiation cycle. The coulombic efficiency increases with increasing cycle number, starting from 86% (2nd cycle) ending at 92% (5th cycle). We also measure the capacity of $LT_{1.8}Z_{0.2}P$ with 69 mA g^{-1}. The plateau positions of lithium insertion and de-insertion are nearly the same, and the capacity is slightly less. $LT_{1.8}Z_{0.2}P$ capacity of the first delithiation plateau is measured ~45 mAh g^{-1} (0.69 mol Li), which drops to 41 mAh g^{-1} (0.63 mol Li) in the second cycle. The two plateau positions of $LT_{1.5}Z_{0.5}P$ and $LT_{1.8}Z_{0.2}P$ are in line with the reported plateaus for LTP at 2.4 V (insertion) and 2.6 V *vs.* Li/Li^+ (de-insertion) [26].

Unfortunately, this potential plateau is considered less important in this study, because the LTZP electrode potential does not have the opportunity to encounter the 2.5 V plateau and undergo lithiation/delithiation at this flat profile [30]. When we operate the $LT_{1.5}Z_{0.5}P$/AC capacitor, the open circuit potentials (OCP) at 0% SOC

are generally below 2.5 V *vs.* Li/Li^+ for both electrodes. OCP at 0% SOC is the starting (also the end) point where the $LT_{1.5}Z_{0.5}P$ and the AC electrode potentials go their separate ways in charge/discharge. The OCP value of the cell is between 2.0 and 1.5 V (*vs.* Li/Li^+) for the 1:1 mass ratio; between 2.4 and 2.0 V (*vs.* Li/Li^+) for the 1:2 mass ratio; 1.6 and 1.4 V (*vs.* Li/Li^+) for the 1:0.5 ratio. The potential of $LT_{1.5}Z_{0.5}P$, being the negative electrode of the hybrid capacitor, descends from a position lower than the 2.5 V plateau, shall not reach the plateau under normal operation conditions. In other words, the $LT_{1.5}Z_{0.5}P$/AC capacitor does not utilize the 2.5 V plateau in energy storage.

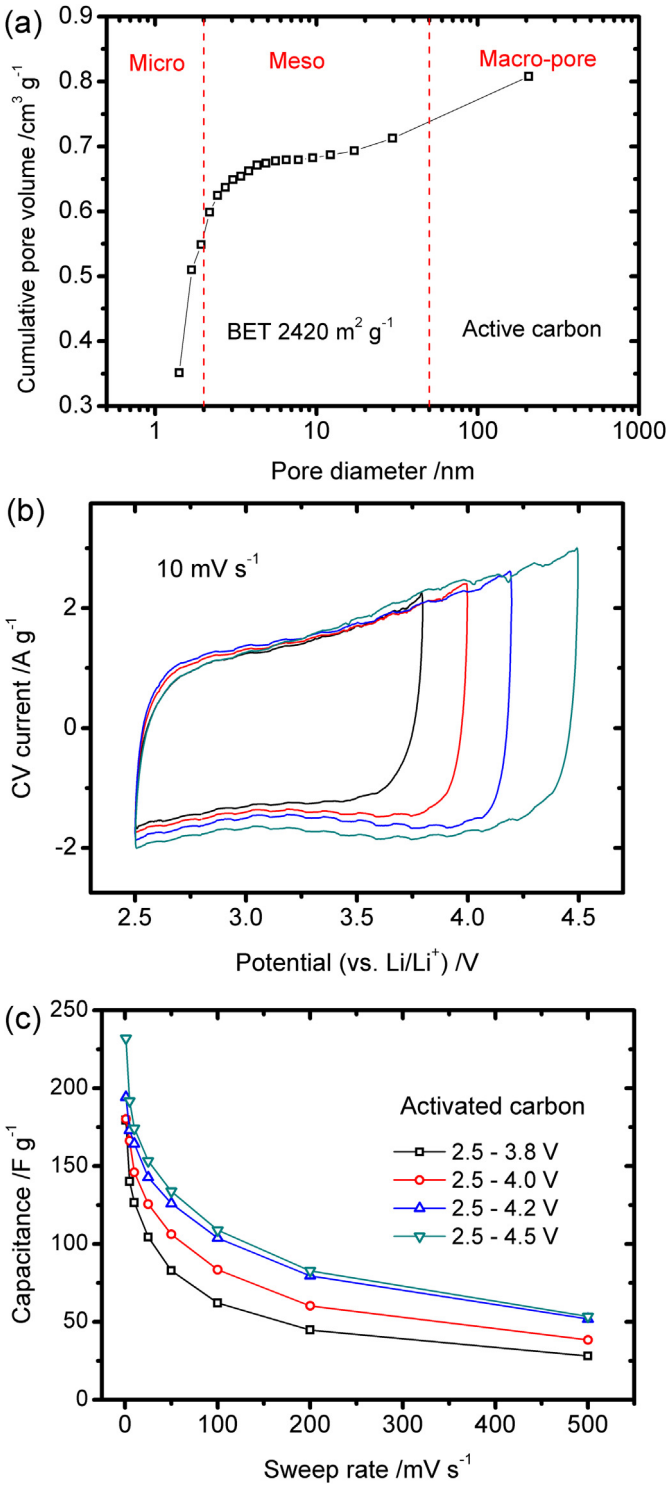

Fig. 3. Properties of activated carbon and electrochemical properties of the AC electrode. (a) The pore size distribution of AC is calculated based on the nitrogen desorption curve. (b) The CV curves are scanned at 10 mV s^{-1} for the AC electrode. (c) The capacitance values of the AC electrode are plotted versus the sweep rate.

Still there is an ample lithium capacity below 2.0 V in $LT_{1.5}Z_{0.5}P$, as illustrated in Fig. 2(b), which shows the lithiation/delithiation behavior of the $Li/LT_{1.5}Z_{0.5}P$ cell between 2.0 and 0.01 V (*vs.* Li/Li^+) at 100 mA g^{-1}. In this potential range, the initial lithiation capacity reaches 431 mAh g^{-1}. The capacity gradually decreases, and arrives at 285 mAh g^{-1} at the 30^{th} cycle. On the other hand, the delithiation capacity of $Li/LT_{1.5}Z_{0.5}P$ is smaller in quantity but more noteworthy, since delithiation of $LT_{1.5}Z_{0.5}P$ corresponds to discharge operation of the negative electrode in an $LT_{1.5}Z_{0.5}P$/AC capacitor. Fig. 2(c) indicates the electrode capacity of $LT_{1.5}Z_{0.5}P$ is 373 mAh g^{-1} at the first cycle, and goes down to 275 mAh g^{-1} at the 30^{th} cycle. In other words, the capacity of the first delithiation cycle approximates 5.7 mol of lithium, while that of the 30^{th} cycle comes near to 4.2 mol of lithium. Fig. 2(c) also presents the coulombic efficiency of $Li/LT_{1.5}Z_{0.5}P$ cell, when operated between 2.0 and 0.01 V (*vs.* Li/Li^+). The coulombic efficiency increases with increasing cycle number, since the capacity difference diminishes between lithiation and delithiation. Initially the efficiency is 86%, rises up to 93% at the 9th cycle, and further increases to 96% in the last six cycles.

Fig. 3(a) presents the pore size distribution of 3J&J grade 4/70 activated carbon, a product through pyrolysis of coconut shells. Evidently, grade 4/70 is a microporous carbon with approximately 70% of its pore volume occupied by the micropores, whose diameters are less than 2 nm according to IUPAC. Based on the BJH method, the average desorption pore diameter is calculated 1.41 nm with a total pore volume 0.8079 cm^3 g^{-1} and a surface area 1660 m^2 g^{-1}. The multipoint BET surface area is evaluated 2420 m^2 g^{-1} for this AC.

Voltammograms of the Li/AC cell are plotted in Fig. 3(b) at sweep rate 10 mV s^{-1}. The CV curves display a nearly rectangular shape without obvious redox peaks, indicating its double-layer capacitance characteristics. These four CVs, with increasing upper potential 3.8, 4.0, 4.2, 4.5 V (*vs.* Li/Li^+), demonstrate that the upper potential end of the rectangular voltammogram is slightly wider than the low potential end. Hence the CV capacitance increases with increasing potential excursion, as shown in Fig. 3(c). These capacitance values are computed using the following formula,

$$C_{CV} = \frac{In_{CV}}{2\nu \times m_a \times \Delta V}, \quad (1)$$

in which In_{CV} is the area integral of the rectangle, ν is the sweep rate, m_a is the active mass of AC electrode, ΔV is the scanned potential window. The CV capacitance value at a low sweep rate can be quite high, ~200 F g^{-1}. Furthermore, we have measured the CV curve up to the upper potential limit 4.7 V (*vs.* Li/Li^+) and note an anodic peak at the edge of this voltammogram, signifying the electrolyte decomposition or ion intercalation. Hence, we specify the cut-off potential for the upper limit of positive AC electrode to be 4.6 V (*vs.* Li/Li^+).

3.2. Analysis of the hybrid capacitor

Before examining the $LT_{1.5}Z_{0.5}P$/AC capacitor in depth, we have assessed three cells of 1:0.5, 1:1, and 1:2 mass ratios. The cell of 1:1 mass ratio exhibits superior power and energy densities. Hence, the following analysis is focused on the 1:1 mass ratio. The power and energy data of these three cells are compared in Fig. S1 of Supporting information.

It is of interest to analyze the individual electrode behavior when the $LT_{1.5}Z_{0.5}P$/AC (1:1) capacitor accepts and delivers energy. Because the positive and the negative electrodes are in series, we expect the slower electrode is rate-determining. Evidently, the rate-determining electrode ought to be $LT_{1.5}Z_{0.5}P$, since the lithiation/delithiation action is slower in rate, compared with the electrostatic response of double-layer AC electrode. In other words, the $LT_{1.5}Z_{0.5}P$ electrode ought to behave in a full cell, just like in a half cell, especially at low specific currents. Figs. 4(a) and 5(a) verify the above speculation, showing the two negative potential profiles resemble the potential profiles of Fig. 2(b). Note that the capacity of Fig. 2(b) is equivalent to lithiation/delithiation time because the specific current is fixed. For example, the negative potential of Fig. 4(a) drops vertically from 2.0 to 1.5 V (*vs.* Li/Li^+), then sketches a slanted curve toward the minimum potential 0.54 V (*vs.* Li/Li^+), no different from the lithiation curve of $LT_{1.5}Z_{0.5}P$ electrode. After the minimum point, the negative potential arises almost linearly and returns to the starting potential, just like the potential variation of $LT_{1.5}Z_{0.5}P$ during delithiation in Fig. 2(b). At 0.07 A g^{-1}, the negative potential of Fig. 5(a) displays similar features in lithiation/delithiation curves of $LT_{1.5}Z_{0.5}P$, even though the scale is different since the voltage window is set 3.4 V instead of 3.0 V. Meanwhile, the AC electrode plays an auxiliary role. Its positive potential profiles, in Figs. 4(a) and 5(a), swiftly respond to variations in the negative potential, therefore, the positive profiles differ significantly from

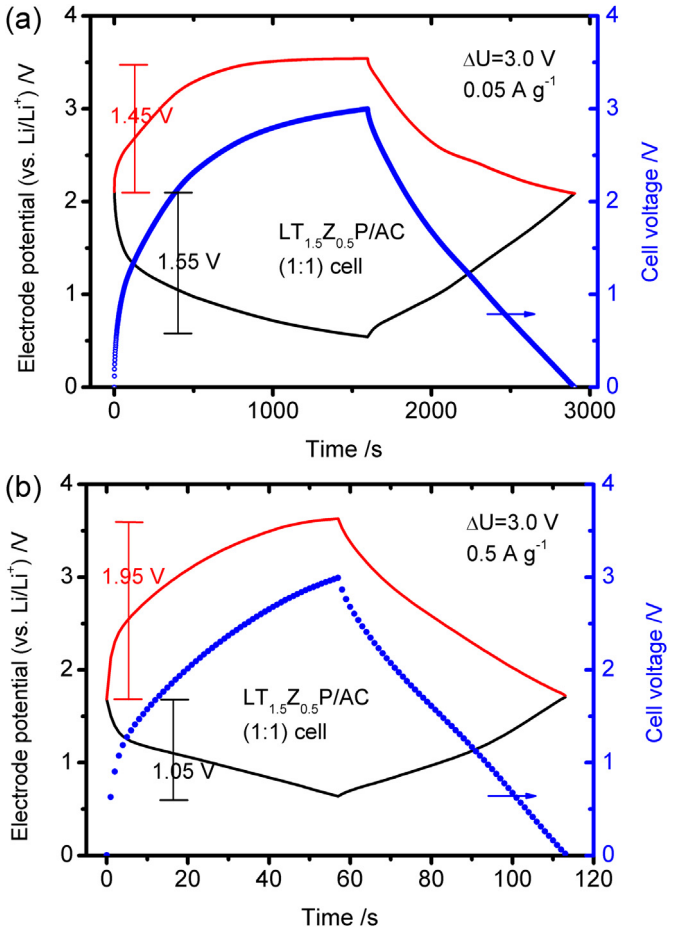

Fig. 4. Cell voltage and electrode potentials during charge/discharge of the $LT_{1.5}Z_{0.5}P$/AC (1:1) capacitor. Data have been taken with ΔU = 3.0 V and current density (a) 0.05 A g^{-1}; (b) 0.5 A g^{-1}. The mass loading of $LT_{1.5}Z_{0.5}P$ is 0.85 mg on the negative electrode; and that of AC is 0.85 mg on the positive electrode.

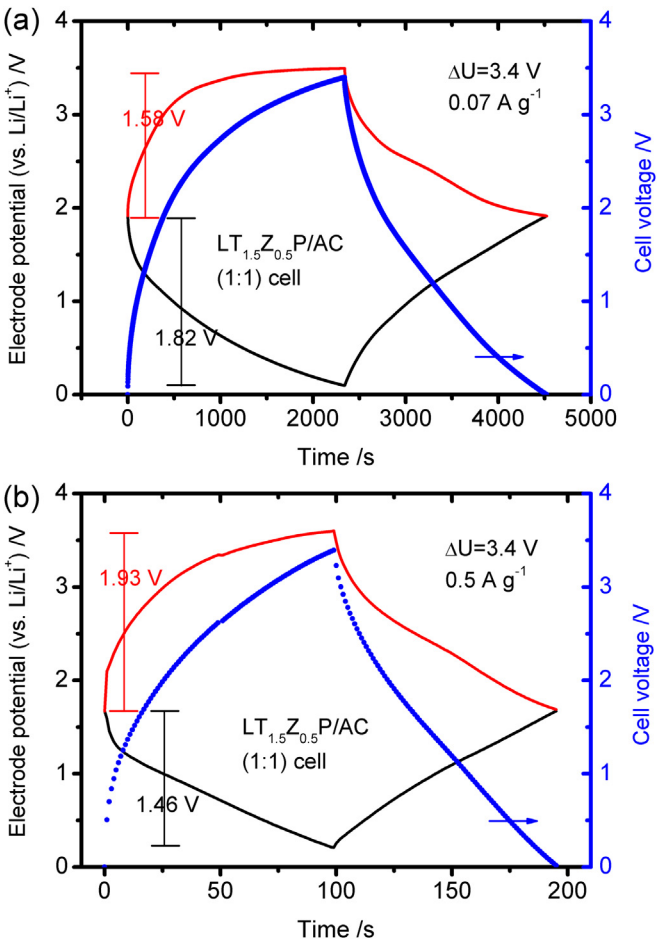

Fig. 5. Cell voltage and electrode potentials during charge/discharge of the $LT_{1.5}Z_{0.5}P$/AC (1:1) capacitor. Data have been taken with ΔU = 3.4 V and current density (a) 0.07 A g^{-1}; (b) 0.5 A g^{-1}. The mass loading of $LT_{1.5}Z_{0.5}P$ is 0.85 mg on the negative electrode; and that of AC is 0.85 mg on the positive electrode.

the typical triangular shape of AC electrode in electrochemical capacitors. We would like to mention another reason for the close resemblance between the negative potential profiles of Fig. 4(a) and the lithiation/delithiation curves of Fig. 2(b). Their specific currents are virtually the same, 50 mA g^{-1} of Fig. 4(a) is based on the mass sum of $LT_{1.5}Z_{0.5}P$ and AC in a 1:1 ratio, equivalent to 100 mA g^{-1} of Fig. 2(b).

We further note that, the position of OCP at 0% SOC, abbreviated as OCP in the following discussion, is important in how the voltage window ΔU is partitioned into positive window ΔU_+ and negative window ΔU_-. At low specific current 0.05 A g^{-1}, Fig. 4(a) shows that the voltage window 3.0 V is almost equally divided into ΔU_+ 1.45 V and ΔU_- 1.55 V, denoting that the positive and the negative electrodes have a similar storage capacity. In the voltage window 3.0 V, the OCP value decreases with increasing specific current; 2.11 V *vs.* Li/Li^+ for 0.05 A g^{-1}, 1.90 V for 0.15 A g^{-1}, 1.68 V for 0.5 A g^{-1}, 1.58 V for 1.0 A g^{-1}. According to Fig. 2(b), the $LT_{1.5}Z_{0.5}P$ capacity varies with the potential, relatively small around 2.0 V (*vs.* Li/Li^+), and becomes much larger when the potential decreases down to 0.5 V (*vs.* Li/Li^+). Because the OCP position is lower at higher specific currents, Fig. 4(b) shows a flat negative potential profile at 0.5 A g^{-1}, and ΔU_- 1.05 V is substantially less than ΔU_+ 1.95 V. When the voltage window is set 3.4 V, we observe a similar decreasing trend in OCP position, 1.92 V (*vs.* Li/Li^+) for 0.07 A g^{-1}, 1.80 V for 0.15 A g^{-1}, 1.67 V for 0.5 A g^{-1}, and 1.56 V for 1.0 A g^{-1}. Therefore, Fig. 5(a)

shows that ΔU_- 1.82 V is larger than ΔU_+ 1.58 V at 0.07 A g^{-1}; while Fig. 5(b) indicates that ΔU_- 1.46 V is less than ΔU_+ 1.93 V at 0.5 A g^{-1}. More data on the positive and negative potential variations during charge/discharge at 0.15 and 1.0 A g^{-1} are given in Figs. S2 and S3. The voltage partitions of $\Delta U = 3.0$ and 3.4 V are summarized in Table S1 of Supporting information.

Voltage partition reveals the relative weight of positive and negative electrode capacities. Under most specific currents in the range 0.03–6.0 A g^{-1}, the negative electrode is more capacitive than the positive electrode, that is, $\Delta U_- < \Delta U_+$. Only at a low specific current, 0.05 A g^{-1} ($\Delta U = 3.0$ V) or 0.07 A g^{-1} ($\Delta U = 3.4$ V), the negative electrode could be less capacitive than the positive electrode. A less capacitive $LT_{1.5}Z_{0.5}P$ electrode occurs since the OCP position is high around 2.0 V *vs.* Li/Li^+. The above discussion applies after repeated cycling as well, even though we did not measure potential profile evolution in negative and positive electrodes after long-term operation. But, judging from the similarity of cell voltage profiles recorded in separate measurements of short-term performance and long-term stability, we infer the above analysis still applies. Thus, we conclude that exploitation of $LT_{1.5}Z_{0.5}P$ capacity depends on the OCP position, and a lower OCP value at high specific currents makes the large $LT_{1.5}Z_{0.5}P$ capacity available.

We calculate the values of power density (P), energy density (E), and cell capacity (Q_{cell}) using discharge curves of the third cycle in running the galvanostatic charge/discharge experiments.

$$E = I\int_{t_i}^{t_f} U(t)\mathrm{d}t, \tag{2}$$

$$P = \frac{E}{\left(t_f - t_i\right)}, \tag{3}$$

$$Q_{cell} = I\left(t_f - t_i\right), \tag{4}$$

where I is the specific current based on the active mass sum of two electrodes, $U(t)$ the cell voltage as a function of time, t_i, t_f are the start time and the end time of cell discharge. Two Ragone plots of the $LT_{1.5}Z_{0.5}P$/AC (1:1) capacitor are plotted in Fig. 6(a) for $\Delta U = 3.0$ and 3.4 V. Intriguingly, the two curves come close to each other in the high power (6.0 A g^{-1}) region. The merging trend is the direct consequence that the $LT_{1.5}Z_{0.5}P$ electrode exploits its large capacity at high specific currents. With an increasingly more capacitive $LT_{1.5}Z_{0.5}P$ (negative) electrode, the hybrid cell capacity is gradually controlled by the AC electrode of the double-layer capacitance, exhibiting more features of the double-layer capacitor. At the other

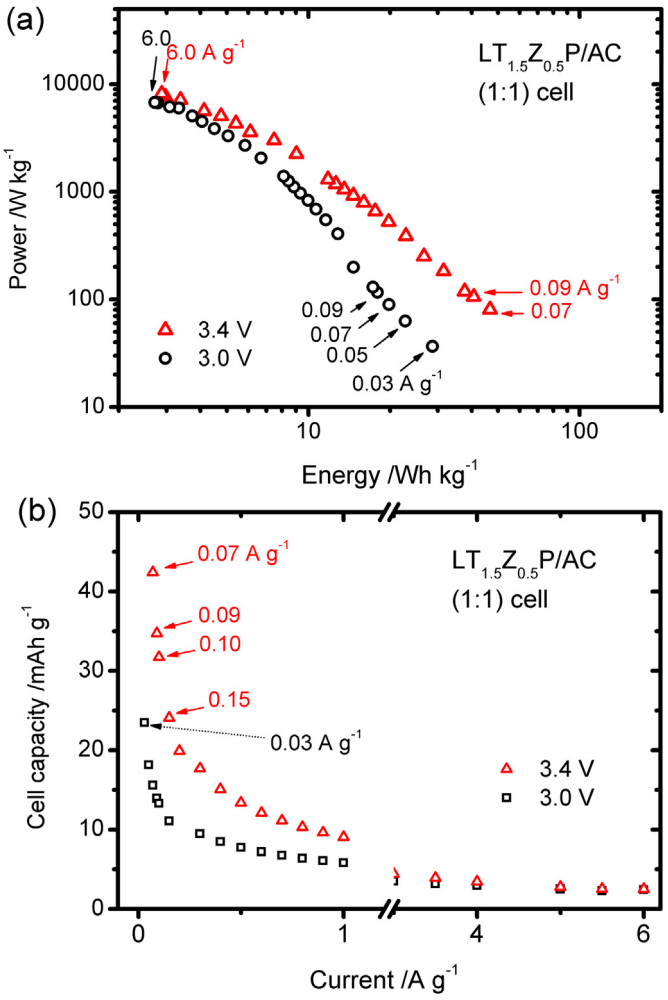

Fig. 6. Ragone plots and cell capacitances of the $LT_{1.5}Z_{0.5}P$/AC (1:1) capacitor. (a) The Ragone plots for $\Delta U = 3.0$ V and 3.4 V. (b) The cell capacitance values versus current density calculated with the discharge curves of galvanostatic charge/discharge tests. Symbolic values of current density are also marked in the graph.

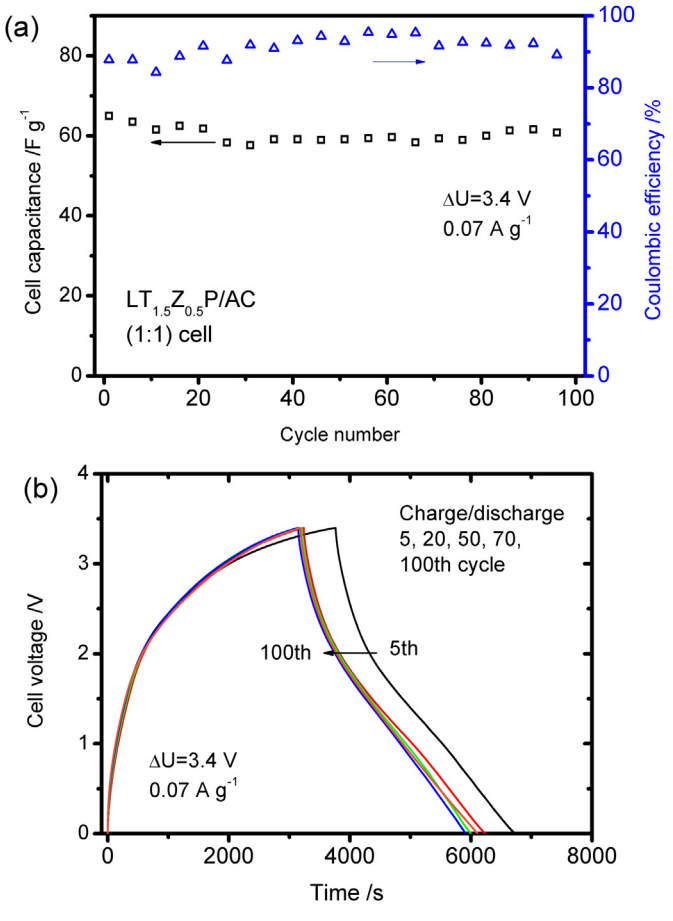

Fig. 7. Cycle stability of the $LT_{1.5}Z_{0.5}P$/AC (1:1) cell with $\Delta U = 3.4$ V and 0.07 A g^{-1}. (a) Values of the cell capacitance and the coulombic efficiency are plotted with respect to the cycle number. (b) The charge/discharge curves of 5, 20, 50, 70, 100th cycles are stacked to show its capacity fading. The cycle stability data were measured with a different cell, not the cell used in recording data of Figs. 4–6.

end, in the low current region, the $LT_{1.5}Z_{0.5}P$ electrode gets more involved in the cell operation, the cell displays more battery-like characteristics. For example, the energy density of 3.4 V is 46.7 Wh kg^{-1}, much higher than 19.8 Wh kg^{-1} of 3.0 V at specific current 0.07 A g^{-1}. Thus, the $LT_{1.5}Z_{0.5}P$/AC (1:1) cell displays more energy at low specific currents.

Fig. 6(b) reveals this trait in terms of charge capacity, Q_{cell}. Fig. 6(b) indicates that the cell capacities are nearly the same for $\Delta U = 3.0$ and 3.4 V at high currents. For example, the cell capacity is 2.42 mAh g^{-1} (3.0 V) and 2.50 mAh g^{-1} (3.4 V) at high current 6.0 A g^{-1}. But, at the low currents, the capacity of 3.4 V is much higher than that of 3.0 V, exemplified by 42.4 mAh g^{-1} (3.4 V) against 15.6 mAh g^{-1} (3.0 V) at 0.07 A g^{-1}. With a voltage window ΔU = 3.4 V, we measure the maximum energy density 46.7 Wh kg^{-1}, and the maximum power density 8.12 kW kg^{-1}.

Fig. 7(a) presents cycle stability of the $LT_{1.5}Z_{0.5}P$/AC (1:1) capacitor that is charged and discharged with $\Delta U = 3.4$ V and mass-specific current 0.07 A g^{-1}. The cell capacitance ($=Q_{cell}/\Delta U$) begins with 65.0 F g^{-1}, decreases to 57.7 F g^{-1} at the 31st cycle, increases slowly to 61.6 F g^{-1} at the 91st cycle, and ends at 60.6 F g^{-1} at the 100th cycle. The capacity retention is 93%. The coulombic efficiency of $\Delta U = 3.4$ V starts from 86%, increases to somewhat higher than 90%, then returns to 90% after 100 cycles. This efficiency is inferior to the typical efficiency of electrochemical capacitor. Two probable causes of relative low efficiency are lithium loss and electrolyte decomposition [31]. Lithium loss of electrodes generally leads to considerable decrease in capacity. Since the capacity retention is high 93% in Fig. 7(a), lithium loss does not seem to be the reason. If the electrolyte decomposes severely, we could observe a colored electrolyte or separator, which was not visible at the end of 100 cycles. We think a mild reductive decomposition of electrolyte might occur at the negative electrode and expend some amount of electricity in formation of the solid electrolyte interface, since the negative potential does drop to a very low value, ~0.1 V (*vs.* Li/Li^+), in charge/discharge. Since the negative electrode experiences the low potential only for a short period, the decomposition extent is finite, resulting in the less ideal efficiency. Fig. 7(b) shows the charge/discharge curves of 5, 20, 50, 70 100^{th} cycle, indicating most of capacity decline occurs within the first 20 cycles. Thus we conclude that the stability and reversibility of $LT_{1.5}Z_{0.5}P$/AC are respectable when operated at low specific current in ΔU = 3.4 V, but certain level of irreversibility exists.

4. Conclusions

We have fabricated a hybrid $LT_{1.5}Z_{0.5}P$/AC lithium ion capacitor with the 1:1 mass ratio and analyzed its performance characteristics. The hybrid capacitor exploits the lithium capacity of $LT_{1.5}Z_{0.5}P$ nanocrystals below its 2.5 V (*vs.* Li/Li^+) plateau during charge/discharge operation. Since the slope of the potential versus capacity curve differs at high or low potential positions for $LT_{1.5}Z_{0.5}P$, the OCP value at 0% SOC exerts significant influences on the capacity of negative electrode. The capacity of negative electrode increases with decreasing OCP value; and the OCP value decreases with increasing current. Consequently, the hybrid cell behaves like an electrochemical capacitor of double layer capacitance at high currents. The hybrid cell exhibits more attributes of the battery-like electrode at low currents.

Acknowledgment

This work is financially supported by the National Science Council of Taiwan through the project MOST 103-2221-E-011-153-MY3. The miscellaneous fees are paid through one of Top University Projects 103H45140 *via* National Taiwan University of Science and Technology.

Appendix A. Supplementary data

Supplementary data related to this article can be found at http://dx.doi.org/10.1016/j.jpowsour.2014.10.047.

References

[1] N. Omar, M. Daowd, O. Hegazy, M. Al Sakka, Th. Coosemans, P. Van den Bossche, J. Van Mierlo, Electrochim. Acta 86 (2012) 305–315.
[2] K. Naoi, S. Ishimoto, J. Miyamoto, W. Naoi, Energy Environ. Sci. 5 (2012) 9363–9373.
[3] K. Naoi, W. Naoi, S. Aoyagi, J. Miyamoto, T. Kamino, Acc. Chem. Res. 46 (2013) 1075–1083.
[4] D. Cericola, P. Novak, A. Wokaun, R. Kotz, Electrochim. Acta 56 (2011) 8403–8411.
[5] D. Cericola, P. Novak, A. Wokaun, R. Kotz, Electrochim. Acta 56 (2011) 1288–1293.
[6] H. Li, L. Cheng, Y. Xia, Electrochem. Solid State Lett. 8 (2005) A433–A436.
[7] S.B. Ma, K.W. Nam, W.S. Yoon, X.Q. Yang, K.Y. Ahn, K.H. Oh, K.B. Kim, Electrochem. Commun. 9 (2007) 2807–2811.
[8] X. Hu, Y.J. Huai, Z. Lin, J.S. Suo, Z.H. Deng, J. Electrochem. Soc. 154 (2007) A1026–A1030.
[9] S. Chen, H. Hu, C. Wang, G. Wang, J. Yin, D. Cao, J. Renewable Sustainable Energy 4 (2012) 033114.
[10] A.D. Pasquier, I. Plitz, J. Gural, F. Badway, G.G. Amatucci, J. Power Sources 136 (2004) 160–170.
[11] L.M. Chen, Q.Y. Lai, Y.J. Hao, J.H. Huang, X.Y. Ji, Ionics 14 (2008) 441–447.
[12] K. Karthikeyan, V. Aravindan, S.B. Lee, I.C. Jang, H.H. Lim, G.J. Park, M. Yoshio, Y.S. Lee, J. Power Sources 195 (2010) 3761–3764.
[13] M.V. Reddy, G.V. Subba Rao, B.V.R. Chowdari, J. Power Sources 195 (2010) 5768–5774.
[14] N. Bockenfeld, A. Balducci, J. Power Sources 235 (2013) 265–273.
[15] H. Zhao, L. Pan, S. Xing, J. Luo, J. Xu, J. Power Sources 222 (2013) 21–31.
[16] J.J. Yang, C.H. Choi, H.B. Seo, H.J. Kim, S.G. Park, Electrochim. Acta 86 (2012) 277–281.
[17] G.G. Amatucci, F. Badway, A.D. Pasquier, T. Zheng, J. Electrochem. Soc. 148 (2001) A930–A939.
[18] A.D. Pasquier, A. Laforgue, P. Simon, G.G. Amatucci, J.F. Fauvarque, J. Electrochem. Soc. 149 (2002) A302–A309.
[19] A.D. Pasquier, A. Laforgue, P. Simon, J. Power Sources 125 (2004) 95–102.
[20] H.S. Choi, J.H. Im, T.H. Kim, J.H. Park, C.R. Park, J. Mater. Chem. 22 (2012) 16986–16993.
[21] T. Aida, K. Yamada, M. Morita, Electrochem. Solid State Lett. 9 (2012) A534–A536.
[22] S.R. Sivakkumar, A.G. Pandolfo, Electrochim. Acta 65 (2012) 280–287.
[23] C. Decaux, G. Lota, E. Raymundo-Pinero, E. Frackowiak, F. Beguin, Electrochim. Acta 86 (2012) 282–286.
[24] K. Arbi, A. Kuhn, J. Sanz, F. Garcia-Alvarado, J. Electrochem. Soc. 157 (2010) A654–A659.
[25] H.S. Kim, H.S. Ahnn, J.H. Lee, Y.K. Sun, C.S. Yoon, J. Electrochem. Soc. 158 (2011) A396–A399.
[26] V. Aravindan, W. Chuiling, M.W. Reddy, G.V.S. Rao, B.V.R. Chowdari, S. Madhavi, Phys. Chem. Chem. Phys. 14 (2012) 5808–5814.
[27] M. Zhou, L. Liu, L. Yi, Z. Yang, S. Mao, Y. Zhou, T. Hu, Y. Yang, B. Shen, X. Wang, J. Power Sources 234 (2013) 292–301.
[28] G.X. Wang, D.H. Bradhurst, S.X. Dou, H.K. Liu, J. Power Sources 124 (2003) 231–236.
[29] K. Arbi, J.M. Rojo, J. Sanz, J. Eur. Ceram. Soc. 27 (2007) 4215–4218.
[30] S. Patoux, C. Masquelier, Chem. Mater. 14 (2002) 5057–5068.
[31] K. Xu, Chem. Rev. 104 (2004) 4303–4417.